

Design of a Metalens for Correcting the Phase Distortions of a Hemispheric Dielectric Radome in the Ka Band

Ezgi Öziş^{1, *}, Andrey V. Osipov¹, and Thomas F. Eibert²

Abstract—Metasheets are ultra-thin sheets built from sub-wavelength resonators designed to achieve certain frequency-dependent transmission behavior. A semianalytical approach based on an equivalent circuit representation is proposed to calculate the microwave transmission through metasheets consisting of two-dimensional periodic arrays of planar circular metal rings on a dielectric substrate. In the semianalytical approach, the impedances of the equivalent circuit are parameterized and fitted to match the values of transmission coefficients obtained by full-wave simulations at selected frequency points. As dimensional parameters, the outer radius and width of the ring are considered. A metalens with four concentric zones is designed by using this semianalytical approach to correct the phase distortions due to a polypropylene hemispheric radome at frequencies around 28 GHz in the Ka band. It is shown that the designed metalens works well for 27 GHz, 28 GHz, 29 GHz, and 29.5 GHz, implying the bandwidth of approximately 2.5 GHz. The field transmitted through the metalens and the radome is calculated by Physical Optics (PO). The electrically large integration area is divided into small square facets to calculate the PO integral. The calculated and measured results are shown to agree well.

1. INTRODUCTION

Radomes protect antennas from environmental effects like rain, snow, wind, and ice. On the one hand, every radome causes distortions in the phase and amplitude of the transmitted fields. For enhancing the performance of the antenna system, the radome should be properly designed according to the type of the application. For correcting the phase of a transmitted wave, the thickness of the radome wall can be changed in different sections [1]. The adjustment of the thickness is not an easy task, particularly for an electrically large radome. For improving the electromagnetic properties of the radome, different types of materials and shapes have been studied. For example, an additional hydrophobic covering of a radome can be used to decrease the losses due to the wet surface of the radome [2].

Metasheets are two-dimensional engineered structures involving a dense array of electrically small particles in a dielectric substrate. The structures, also called metalenses, permit controlling the direction, phase and amplitude of the transmitted wave, shaping the beam and improving the gain of the enclosed antenna [3]. Metalenses are available for increasing the gain, optimizing the return loss [4], high-quality imaging beyond the diffraction limit [5, 6], improving the communication capacity in nanophotonic systems [7], regulating the radius of the vortex beam in the microwave region [8], controlling the phase of transmission and/or reflection in broadband microwave applications [9] and collimating microwave radiation from an antenna [10]. The electromagnetic properties of microwave radomes can be enhanced with metasheets when the conventional lenses cannot be used, for example because of a too large volume and weight. Interesting applications in the Ka band, e.g., [11–13], suggest the need for further studies of the corresponding radomes.

Received 5 November 2019, Accepted 23 December 2019, Scheduled 3 March 2020

* Corresponding author: Ezgi Öziş (ezgi.oezis@dlr.de).

¹ Microwaves and Radar Institute, German Aerospace Center (DLR), Oberpfaffenhofen, Germany. ² Chair of High-Frequency Engineering, Department of Electrical and Computer Engineering, Technical University of Munich, Munich, Germany.

In this study, a metalens is designed to correct the phase distortions caused by a hemispheric radome in the Ka band (between 26.5 and 40 GHz). The metalens consists of concentric circular zones, where the dimensions of the resonators are different. The design is inspired by the well-known Fresnel lens. As it is known, a Fresnel lens consists of a set of concentric annular sections of the same curvature as the standard lens but with reduced thickness and with stepwise discontinuities between them, e.g., [14, 15].

In our design, the thickness of the lens is constant, and only one type of the dielectric substrate is used. Copper circular rings with varying radii are used as resonant inclusions. Linear polarization and normally incident waves are considered. In this study, the semianalytical method based on an equivalent circuit model [16] is generalized to include two geometrical parameters of the resonator in the design of the metalens. For the calculation of the phase distortion upon the transmission through the radome, a ray tracing algorithm is used. The Physical Optics (PO) approximation is applied to calculate the electric field transmitted through the metalens and the radome. The metalens and radome have been manufactured and measured. The results of the PO calculation and of measurements are compared. The extended semianalytical approach for two parameters is explained in Section 2. The metalens design is presented in Section 3. The PO calculation and the approximations in this calculation are described in Section 4. The measured and calculated results are compared in Section 5. The conclusion is given in Section 6. Throughout the paper, a time dependence $e^{j\omega t}$ with angular frequency ω is assumed and suppressed.

2. SEMIANALYTICAL APPROACH WITH TWO DIMENSIONAL PARAMETERS FOR AN INFINITE PLANAR ARRAY OF RESONATORS

The semianalytical approach described in [16] can be used for differently shaped planar particles and according to the shape of the particle, different dimensional parameters can be used. In this study, the main principle of the semianalytical method is still valid but the number of dimensional parameters is now equal to two, and these parameters are the outer radius r_{out} and the width of the ring

$$w = r_{out} - r_i, \quad (1)$$

where r_i is the inner radius. The normalized width is defined by

$$w_n = \frac{w}{p}, \quad (2)$$

and the normalized outer radius by

$$r_n = \frac{r_{out}}{p}, \quad (3)$$

where p is the unit-cell length. The transmission coefficient for the metasheet can be expressed as

$$T = \frac{(q_1 + 1)(q_2 + 1)e^{-k\ell_2(\alpha + j(\beta - 1))}}{1 + q_1 q_2 e^{-2k\ell_2(\alpha + j\beta)}}, \quad (4)$$

where $\alpha = \frac{\sqrt{\varepsilon_r' \tan \delta}}{2}$, $\beta = \sqrt{\varepsilon_r'}$, l_2 is the thickness of the substrate, and k is the free-space propagation constant ($k = \frac{2\pi}{\lambda}$) [16]. The parameters q_1 and q_2 are the internal reflection coefficients at the interfaces between the array of rings and the dielectric layer and between the dielectric layer and free space (vacuum), respectively. The internal reflection coefficients are written in terms of normalized impedances as it is explained in [16]. Transmission blockage occurs when both the real and imaginary parts of transmission coefficient become zero, which leads to the condition for the normalized propagation constant [16]

$$k_{nor}^2 = F_3 = \frac{F_2}{F_1}, \quad (5)$$

where $k_{nor} = kp$. The material of the ring is copper. The thickness of the ring is 0.018 mm. The frequency range is between 18 GHz and 46 GHz.

The dielectric substrate is Megtron6. The thickness of the substrate is 2 mm. The periodicity p is 3 mm. The same simulation setup in ANSYS HFSS is used as in [16]. The material of the airbox is vacuum. The length of the airbox l between the Floquet ports is 50 mm. To extract the phase

of the transmission coefficient, the simulation data S_{21} is multiplied by e^{jkl} to eliminate the airbox effect on the phase. The relative permittivity of the dielectric substrate has been measured with a free-space method to compute the reflection coefficient of the substrate. The infinite planar dielectric substrate has been simulated in HFSS to find the relative permittivity by matching the simulated and the measured reflection coefficients with the result that the relative permittivity of the substrate is 4.33 and the dielectric loss tangent of the substrate is 0.006. The transmission blockage frequency depends only on the ratio of F_2 and F_1 [16]. The presence of a dielectric substrate may dramatically affect the blockage frequency; therefore, the fittings are done on F_1 and F_3 . The expressions for F_1 and F_3 used in [16] should be rewritten because of the additional dimensional parameter (width). The transmission coefficient is determined from F_1, F_2, F_3 as explained in [16]. The four different width values 0.1 mm, 0.13 mm, 0.16 mm, and 0.19 mm are used in the fitting. For each width, five different outer radii 0.9 mm, 1 mm, 1.1 mm, 1.2 mm, and 1.3 mm are chosen. F_1 and F_2 are unitless functions of dimensional parameters [16]. The fitting of the free parameters F_1 and F_2 is done by the curve fitting tool in Matlab for the full-wave simulated amplitude of S_{21} in [16]. Tables 1, 2, 3 and 4 display the calculated values of F_1 and F_2 for the selected values of r_{in} and w .

The parameters F_1 and F_3 can be approximated by exponential functions of the normalized parameters r_n and w_n as

$$F_1(r_n, w_n) = A_1 e^{c_1(w_n)r_n} + B_1 e^{d_1(w_n)r_n} \tag{6}$$

$$F_3(r_n, w_n) = A_3 e^{c_3(w_n)r_n} + B_3 e^{d_3(w_n)r_n}, \tag{7}$$

where the coefficients $c_1, c_3, d_1,$ and d_3 depend on w_n , and the coefficients A_1, A_3, B_1 and B_3 are constant coefficients.

Approximating the arguments of the exponential functions in Eqs. (6) and (7) by the first two

Table 1. Parameters F_1 and F_2 for several values of inner radius (width 0.1 mm).

| r_i (mm) | F_1 | F_2 |
|------------|--------|--------|
| 1.2 | 0.3151 | 0.8407 |
| 1.1 | 0.3340 | 1.1260 |
| 1.0 | 0.3653 | 1.5310 |
| 0.9 | 0.4067 | 2.0990 |
| 0.8 | 0.4668 | 2.9520 |

Table 2. Parameters F_1 and F_2 for several values of the inner radius (width 0.13 mm).

| r_i (mm) | F_1 | F_2 |
|------------|--------|--------|
| 1.17 | 0.2936 | 0.8261 |
| 1.07 | 0.3130 | 1.1090 |
| 0.97 | 0.3415 | 1.5070 |
| 0.87 | 0.3809 | 2.0650 |
| 0.77 | 0.4375 | 2.8920 |

Table 3. Parameters F_1 and F_2 for several values of the inner radius (width 0.16 mm).

| r_i (mm) | F_1 | F_2 |
|------------|--------|-------|
| 1.14 | 0.2749 | 0.806 |
| 1.04 | 0.2936 | 1.093 |
| 0.94 | 0.3205 | 1.484 |
| 0.84 | 0.3587 | 2.036 |
| 0.74 | 0.4135 | 2.859 |

Table 4. Parameters F_1 and F_2 for several values of the inner radius (width 0.19 mm).

| r_i (mm) | F_1 | F_2 |
|------------|--------|--------|
| 1.11 | 0.2588 | 0.7958 |
| 1.01 | 0.2777 | 1.0860 |
| 0.91 | 0.3018 | 1.4660 |
| 0.81 | 0.3397 | 2.0220 |
| 0.71 | 0.3918 | 2.8300 |

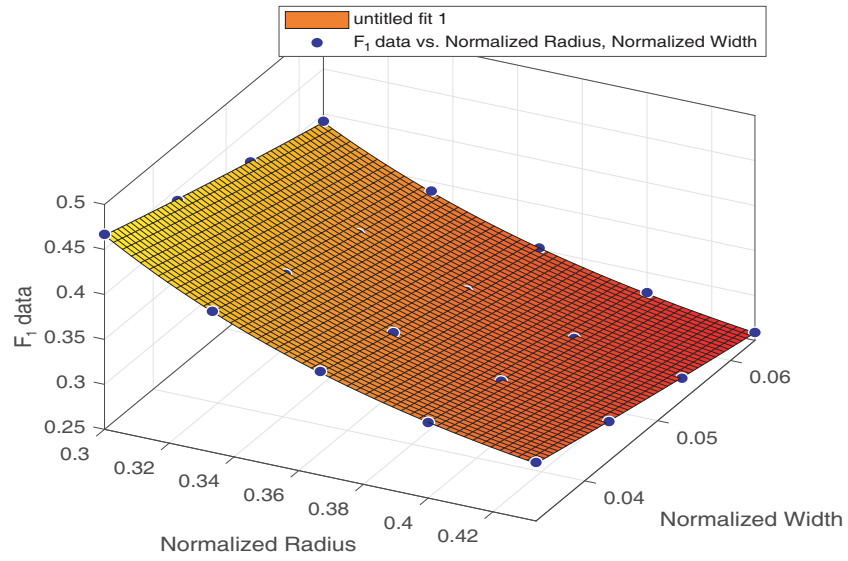


Figure 1. Surface fitting results for the F_1 data.

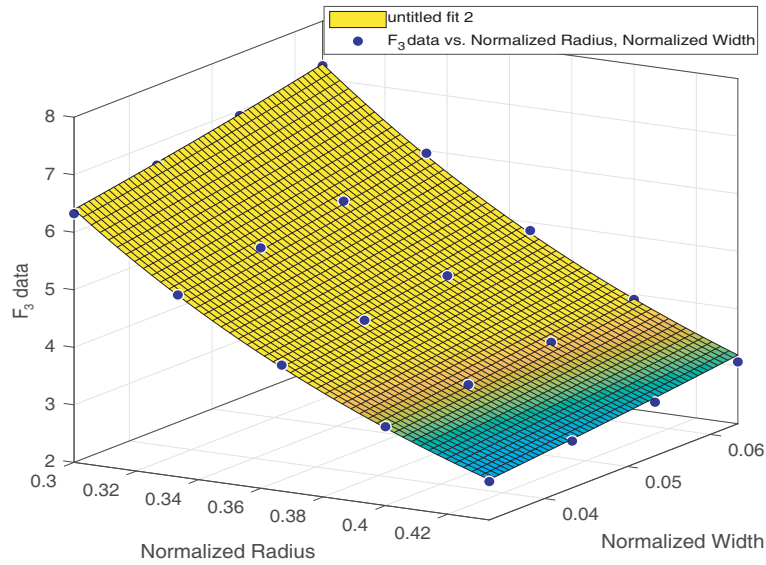


Figure 2. Surface fitting results for the F_3 data.

terms of their Taylor series gives the formulas

$$F_1(r_n, w_n) = A_1 e^{c_{11}r_n + c_{12}r_n w_n} + B_1 e^{d_{11}r_n + d_{12}r_n w_n}, \quad (8)$$

$$F_3(r_n, w_n) = A_3 e^{c_{31}r_n + c_{32}r_n w_n} + B_3 e^{d_{31}r_n + d_{32}r_n w_n}. \quad (9)$$

For calculating the coefficients in Eqs. (8) and (9), the calculated values of F_1 and F_3 for each width value are arranged in matrix form, and the Matlab curve fitting tool is applied to this matrix. For the fitting algorithm, the Levenberg-Marquardt algorithm is chosen. The coefficients are not unique. When the fitting algorithm is changed, the values of the coefficients may slightly change. The functions in Eqs. (8) and (9) are fitted on the exact data for F_1 and F_3 (Tables 1, 2, 3 and 4) with a good agreement as seen in Figs. 1 and 2. The calculated coefficients of the exponential functions are presented in Tables 5 and 6.

Table 5. Values of the coefficients in the approximation in Eq. (8).

| Coefficients | F_1 |
|--------------|----------|
| A_1 | 0.1991 |
| B_1 | 4.0640 |
| c_{11} | 0.9071 |
| c_{12} | -11.9200 |
| d_{11} | -8.595 |
| d_{12} | -27.69 |

Table 6. Values of the coefficients in the approximation in Eq. (9).

| Coefficients | F_3 |
|--------------|---------|
| A_3 | 43.190 |
| B_3 | 3.754 |
| c_{31} | -6.789 |
| c_{32} | 11.410 |
| d_{31} | -17.060 |
| d_{32} | 128.100 |

3. METALENS DESIGN

By using this extended semianalytical approach, the metalens will be designed. We have studied a hemispheric radome from polypropylen (PP) with the measured relative permittivity 2.242, and dielectric tangent loss is 0.001. The thickness of the radome is 5 mm. The inner diameter of the radome is 190 mm. The metasheet is located at the basis of the radome (Fig. 3). Even for a plane wave propagating along the symmetry axis, the incidence angle varies across the curved radome surface, which results in the distortion of the wave upon transmission through the radome. The metalens is designed to correct the phase of the transmitted wave, i.e., to make the wave front plane again. Since the refractive index of PP is almost real-valued and only slightly different from unity, attenuation and multiple reflections in the radome wall are neglected. Multiple reflections between the radome and the metalens can also be neglected because of a good transparency of the lens. For an obliquely incident plane wave, additional reflections in the interior of the radome could occur.

The metasheet is divided into 4 zones (Fig. 4). On the one hand, too many zones will result in too narrow zones which can not be homogenized. On the other hand, a too small number of the zones will lead to large phase jumps between the zones. The width of each zone is different. The largest one is the

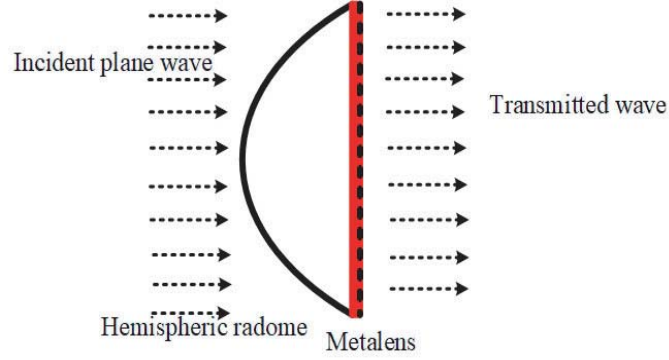


Figure 3. A hemispheric dielectric radome, a metalens at its basis and the direction of incidence of a plane wave.

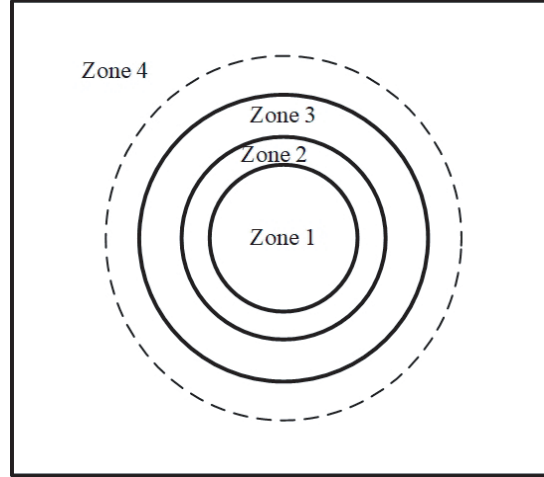


Figure 4. Metalens with four zones; the dashed line shows the position of the radome.

middle zone because the zones, which are close to the rim of the radome, should be small to compensate the faster phase variation. The design frequency is 28 GHz. The phase distribution along the diameter of the radome is calculated in Matlab by a ray tracing algorithm from [17]. The small imaginary part of the dielectric constant is neglected in the calculation because it does not influence the phase of the transmission coefficient.

The propagation of the ray in free space and through the radome is shown in Fig. 5. In the ray optical approximation, the transmission coefficient can be written as

$$T_{\text{radome}} = \frac{e^{jk|AB|}T_{12}e^{jk_d|BC|}T_{21}e^{jk|CD|}}{e^{jk|AE|}}, \quad (10)$$

where T_{12} is the transmission coefficient from medium 1 to medium 2 in Fig. 5; T_{21} is the transmission coefficient from medium 2 to medium 1; and k_d is the propagation constant in the radome medium. The distances $|AB|$, $|BC|$, $|CD|$, and $|AE|$ are shown in Fig. 5. $|AE|$ is the distance between the source and the ground without radome. These transmission coefficients are found by using the Fresnel equations. The deviation of T_{radome} from a constant value is the distortion of the phase of the transmitted wave. In the absence of the radome, the ray from A would propagate parallel to the axis AE . In the presence of the radome, the ray is refracted to point D .

To correct the distortion of the transmitted wave, the zones are realized as metasheets filled with differently sized metal rings. For determining the values of the outer radius and the width of the metal rings, the semianalytical method described in Section 2 is used. The unit-cell is 3 mm at each zone.

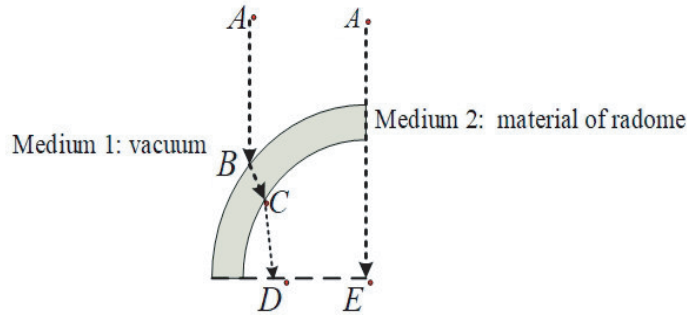


Figure 5. The transmitted rays are no longer parallel because of the curvature of the radome surface.

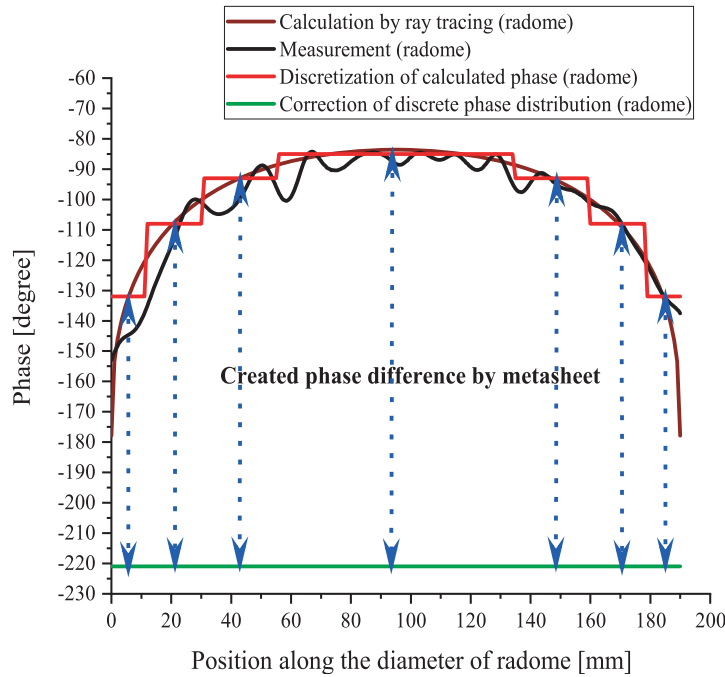


Figure 6. Comparison of calculated and measured phase values at 28 GHz and the expected constant phase value upon the phase compensation by the metalens.

The measured and calculated phase values along the basis of the radome are shown in Fig. 6, and they match with each other. The distance between the basis of the radome and the receiving antenna is 10 cm in this measurement. For the metalens design, the phase distribution is discretized as a step function. The phase values rapidly change when the observation point moves closer to the rim of the radome. The calculated phase distribution is divided as given in Table 7.

The arithmetic average of the phase variation within each zone is calculated and used in the

Table 7. Division of the calculated phase distribution in four zones.

| Position along the radius (mm) | Phase range for each zone (degree) |
|--------------------------------|------------------------------------|
| 95–56 | from –83.55 to –88.44 |
| 55–31 | from –88.72 to –99.38 |
| 30–12 | from –100.05 to –119.00 |
| 11–0 | from –120.70 to –146.40 |

Table 8. The averaged phase values at the basis of the radome and the phase values upon transmission through the metalens by the semianalytical method to correct the phase distortion.

| Position along the radius (mm) | Phase at the basis of radome (degree) | Calculated phase of metalens (degree) |
|--------------------------------|---------------------------------------|---------------------------------------|
| 95–56 | $-85.15 \approx -85$ | -136.5998 |
| 55–31 | $-93.35 \approx -93$ | -127.3648 |
| 30–12 | $-108.25 \approx -108$ | -113.3710 |
| 11–0 | $-131.48 \approx -132$ | -88.9739 |

Table 9. Dimensions of rings to correct the phase distortion.

| Position along the radius (mm) | Outer radius (mm) | Inner radius (mm) |
|--------------------------------|-------------------|-------------------|
| 95–56 | 1.1 | 0.94 |
| 55–31 | 1.07 | 0.91 |
| 30–12 | 1.03 | 0.84 |
| 11–0 | 0.9 | 0.71 |

Table 10. Calculated transmission coefficient by semianalytical approach.

| Position along the radius (mm) | Calculated transmission coefficient at 28 GHz |
|--------------------------------|---|
| 95–56 | $-0.4905 - j0.4638$ |
| 55–31 | $-0.4727 - j0.6190$ |
| 30–12 | $-0.3558 - j0.8233$ |
| 11–0 | $0.0174 - j0.9728$ |

design of the metalens (see the middle column of Table 8). The discretized phase distribution and the expected constant phase upon the combination of the metasheet with the radome are shown in Fig. 6. Table 8 presents the phase distribution from the center (95 mm) to the wall of the radome (0 mm). The outer and inner radius values of rings for each zone of the metalens are calculated by the extended semianalytical method and presented in Table 9. The values of the transmission coefficients calculated by the semianalytical method are shown in Table 10. These values of the complex transmission coefficients are used in the PO integration, which is explained in Section 4.

4. PO METHOD FOR TRANSMISSION THROUGH PLANAR METALENSES

Physical Optics is a well-known high-frequency method for the calculation of scattered and radiated fields by integrating equivalent current densities. The exact current densities on the scattering surface or on the radiating aperture are not known in advance, and the Geometrical Optics approximation is used to determine them. The PO approximation works well for electrically large structures. The main difficulty is that the standard methods of numerical integration may give inaccurate results, and special integration techniques have to be developed, e.g., [18] and [19]. A well-known approach is that the integration area is divided into small planar facets, and a first-order polynomial approximation is applied to the argument of the exponential function [20–22].

In the following PO calculation, the same assumptions as in [23] are made. The difference is that the surface integral is calculated by summation of contributions from subdomains. An incident plane wave with a unit amplitude propagates along the symmetry axis of the radome (Fig. 5). The field transmitted through an aperture Ω , which is in our case the basis of the radome closed with the metalens, can be

expressed in the PO approximation as [24]

$$\mathbf{E}(\mathbf{r})_{tr} = \frac{jk}{4\pi} \iint_{\Omega} g(\mathbf{r}, \mathbf{r}_1) \mathbf{c}(\mathbf{r}, \mathbf{r}_1) d\Omega, \quad (11)$$

where $\mathbf{c}(\mathbf{r}, \mathbf{r}_1) = \hat{s}_1 \times \mathbf{J}_M(\mathbf{r}_1) + Z_0 \hat{s}_1 \times \hat{s}_1 \times \mathbf{J}_E(\mathbf{r}_1)$, \mathbf{J}_M and \mathbf{J}_E are equivalent magnetic and electric surface current densities, which are calculated from the incident field and the transmission coefficient. $Z_0 = \sqrt{\frac{\mu_0}{\epsilon_0}}$ is the free space impedance, and the unit vector \hat{s}_1 pointing from the integration point \mathbf{r}_1 to the observation point \mathbf{r} is given by

$$\hat{s}_1 = \frac{\mathbf{r} - \mathbf{r}_1}{|\mathbf{r} - \mathbf{r}_1|}. \quad (12)$$

The Green's function is

$$g(\mathbf{r}, \mathbf{r}_1) = \frac{e^{-jk|\mathbf{r}-\mathbf{r}_1|}}{|\mathbf{r} - \mathbf{r}_1|} \quad (13)$$

and $|\mathbf{r} - \mathbf{r}_1|$ is the distance between the integration point \mathbf{r}_1 and observation point \mathbf{r} (Fig. 7). The thickness of the metasheet is neglected, therefore $z_1 = 0$. The integration region Ω is subdivided into sufficiently small square facets. With this calculation approach, the function $\frac{\mathbf{c}(\mathbf{r}, \mathbf{r}_1)}{|\mathbf{r}-\mathbf{r}_1|}$ can be assumed constant at each facet, and only the exponential factor is to be integrated in Eq. (11). The transmission coefficient, which is required for the calculation of the equivalent currents in the Geometrical Optics approximation, is a product of T_{radome} and the homogenized transmission coefficients of the metasheet zones, calculated by the semianalytical approach described in Section 2.

The argument of the exponential function is expanded in a Taylor series, and since the facets are small, only the first terms are included [25, 26]

$$\mathbf{E}(\mathbf{r})_{tr} = \frac{jk}{4\pi} \iint_{\Omega} \frac{e^{-jk|\mathbf{r}-\mathbf{r}_1|}}{|\mathbf{r} - \mathbf{r}_1|} \mathbf{c}(\mathbf{r}, \mathbf{r}_1) d\Omega = \frac{jk}{4\pi} \sum_n \frac{\mathbf{c}(\mathbf{r}, \mathbf{r}_{cn})}{|\mathbf{r} - \mathbf{r}_{cn}|} \iint_{\Omega_n} e^{-jk|\mathbf{r}-\mathbf{r}_1|} d\Omega. \quad (14)$$

The surface integral over the flat facet Ω_n can be analytically calculated as

$$\iint_{\Omega_n} e^{-jk|\mathbf{r}-\mathbf{r}_1|} d\Omega \cong a_n b_n \text{sinc} \left(\frac{k}{2} (\hat{s}_{cn}, \mathbf{r}_{2n} - \mathbf{r}_{1n}) \right) \text{sinc} \left(\frac{k}{2} (\hat{s}_{cn}, \mathbf{r}_{3n} - \mathbf{r}_{2n}) \right) e^{-jk|\mathbf{r}-\mathbf{r}_{cn}|}, \quad (15)$$

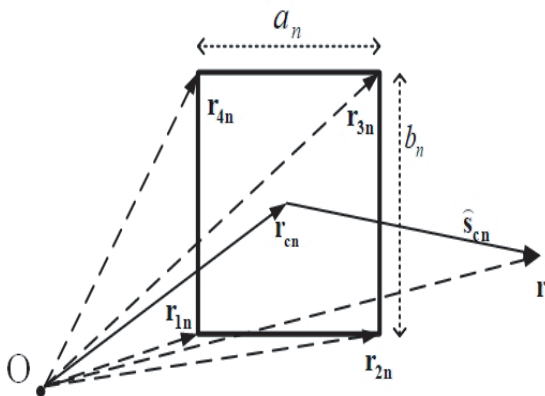


Figure 7. A rectangular facet Ω_n , the origin of a coordinate system and the observation point \mathbf{r} .

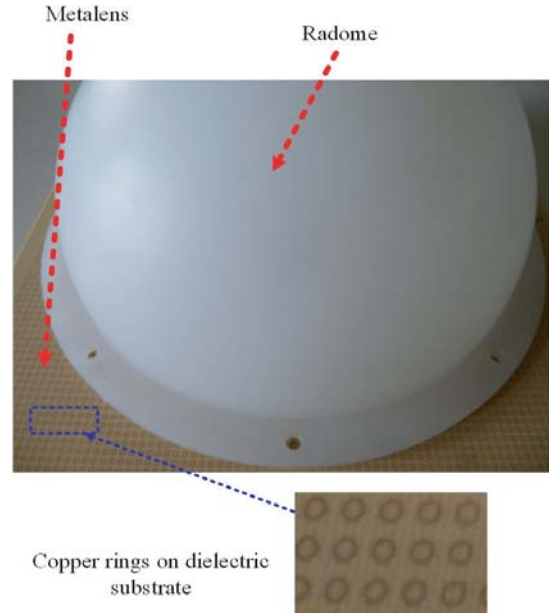


Figure 8. Manufactured metalens is positioned at the basis of the radome.

where $\hat{s}_{cn} = \frac{\mathbf{r} - \mathbf{r}_{cn}}{|\mathbf{r} - \mathbf{r}_{cn}|}$ is the unit vector; $\mathbf{r}_{cn} = \frac{1}{4}(\mathbf{r}_{1n} + \mathbf{r}_{2n} + \mathbf{r}_{3n} + \mathbf{r}_{4n})$ is the center of the facet; and \mathbf{r}_{1n} , \mathbf{r}_{2n} , \mathbf{r}_{3n} , \mathbf{r}_{4n} are the tip points of the facet (Fig. 7). If the facet is square, then $a_n = b_n$, where a_n and b_n are the lengths of the sides.

The radome and metasheet are positioned on a circular aperture in an impenetrable screen (holder covered with an absorber). This means that the transmission coefficient of the screen outside the aperture is zero, which is accounted for in the PO calculation. The receiving antenna is located 6 cm behind the aperture and is moved parallel to the basis of the radome. It is sufficient to scan along one axis because the radome and the metasheet are rotationally symmetric. In the calculation, the amplitude of the incident plane wave is assumed to be unity. The field transmitted through the radome is calculated by ray tracing, and this is the field illuminating the metalens. The field transmitted through the metalens is calculated by multiplication with the homogenized transmission coefficient of the respective metalens zone. Without the metalens at the basis of the radome, the value of the transmission coefficient is 1. A Matlab spline interpolation function is used to calculate the transmitted field on the basis of the radome from a set of values at discrete points along the radius of the radome. The PO calculation has been carried out in Matlab.

5. COMPARISON WITH MEASUREMENTS

In this section, the measured and calculated results are compared. The measurements have been conducted at the Microwaves and Radar Institute of the German Aerospace Center in Oberpfaffenhofen. The measurement setup is described below. This comparison helps to estimate the accuracy of the PO calculation and validates the design. The metasheet is located at the basis of the radome as shown in Fig. 8. The distance between the metasheet and the probe is 6 cm, and the probe has been moved parallel to the radome basis over the distance 200 mm. The holder is used to keep the radome and/or metasheet in a fixed position. Measurements were performed for four cases. First, the radome is placed in the holder. Second, the radome and the metasheet are placed in the holder. Third, only the holder is present. Fourth, the measurement is done in free space, i.e., without radome, metalens and holder. For keeping the continuity of the phase values, 360° is added or subtracted. A dielectric lens has been placed between a transmitting antenna and the radome to convert the antenna beam into a

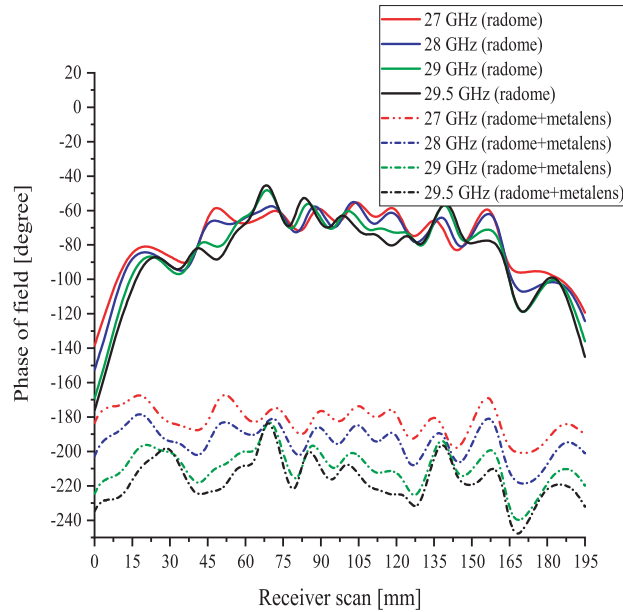


Figure 9. Measured phase values of the field transmitted through the radome with and without metalens at three different frequencies.

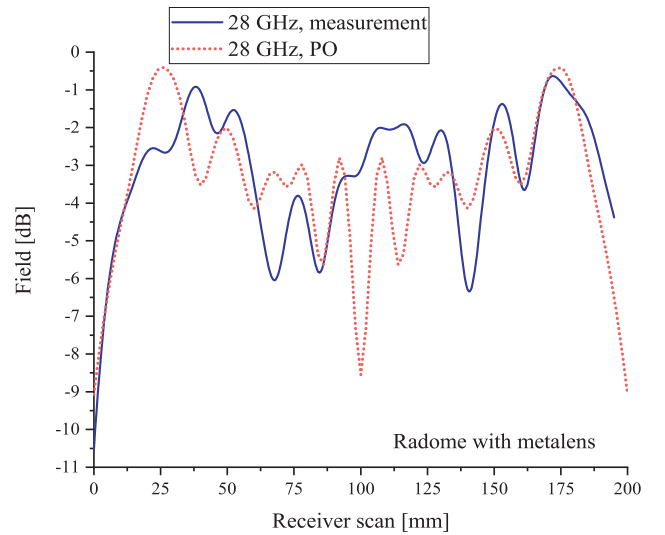


Figure 10. Comparison of the measured and calculated amplitudes of the fields transmitted through the radome and the metalens at 28 GHz.

plane wave. As observed in Fig. 9, the metalens compensates the position-dependent phase distortion of the wave transmitted through the radome, making the phase almost constant over the radome basis. The metalens has been shown to work well for 27 GHz, 28 GHz, 29 GHz and 29.5 GHz, implying the bandwidth of approximately 2.5 GHz. The amplitudes of the calculated and measured fields match well as seen in Fig. 10. There is also a good agreement between measured and calculated phase values as shown in Figs. 11 and 12.

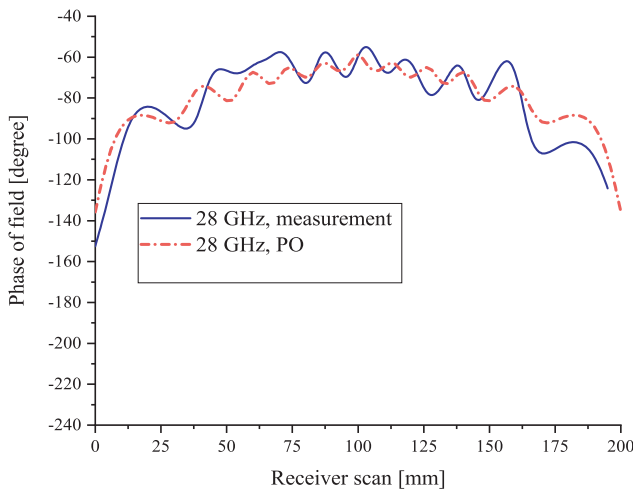


Figure 11. Measured and calculated phases for the radome without metalens at 28 GHz.

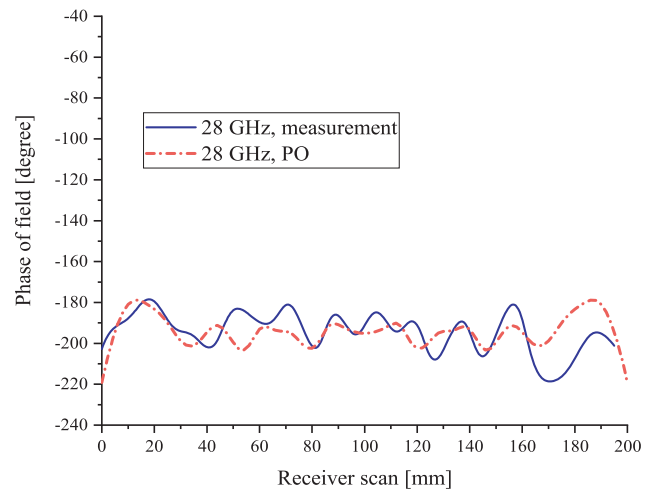


Figure 12. Measured and calculated phases for the radome and metalens at 28 GHz.

6. CONCLUSION

The main result of this work is a simulation method for the design of a metalens to compensate the phase distortion due to a hemispheric radome. The results of performed calculations and measurements have shown that a designed metalens works well to correct the phase distortion. The employed semianalytical approach helps to optimize the metasheet design with very few full-wave numerical simulations. It has been shown that the PO method can be used to estimate the electromagnetic fields transmitted through electrically large inhomogeneous metamaterial structures. In the PO calculation, the integration region is subdivided into smaller regions, at which the linear approximation of the phase factor is applicable, to calculate the PO integral efficiently over electrically large metamaterial apertures.

REFERENCES

1. Meng, H. and W. Dou, *Analysis and Design of Radome in Millimeter Wave Band, Microwave and Millimeter Wave Technologies*, Igor Minin, IntechOpen, 2010, doi: 10.5772/9054, available from: <https://www.intechopen.com/books/microwave-and-millimeter-wave-technologies-from-phonic-bandgap-devices-to-antenna-and-applications/analysis-and-design-of-radome-in-millimeter-wave-band>.
2. Gorgucci, E., R. Bechini, L. Baldini, R. Cremonini, and V. Chandrasekar, "The influence of antenna radome on weather radar calibration and its real-time assessment," *Journal of Atmospheric and Oceanic Technology*, Vol. 30, No. 4, 676–689, 2013.
3. Asadchy, V. S., I. A. Faniayeu, Y. Ra'di, S. A. Khakhomov, I. V. Semchenko, and S. A. Tretyakov, "Broadband reflectionless metasheets: Frequency-selective transmission and perfect absorption," *Phys. Rev. X*, Vol. 5, No. 3, 031005, 2015, doi: 10.1103/PhysRevX.5.031005.
4. Werner, D. H., *Broadband Metamaterials in Electromagnetics: Technology and Applications*, Chapter 1, Pan Stanford, Singapore, 2017.

5. Culhaoglu, E. A., V. A. Osipov, and P. Russer, "Imaging by a double negative metamaterial slab excited with an arbitrarily oriented dipole," *Radio Science*, Vol. 49, 68–79, 2014.
6. She, A., S. Zhang, S. Shian, D. R. Clarke, and F. Capasso, "Large area metalenses: Design, characterization, and mass manufacturing," *Opt. Express*, Vol. 26, 1573–1585, 2018.
7. Khorasaninejad, M., T. W. Chen, C. R. Devlin, J. Oh, Y. A. Zhu, and F. Capasso, "Metalenses at visible wavelengths: Diffraction-limited focusing and subwavelength resolution imaging," *Science*, Vol. 352, No. 6290, 1190–1194, 2016.
8. Zhang, K., Y. Yuan, and Q. Wu, "Metalens in microwave region for the generation of orbital angular momentum," *IEEE International Symposium on Electromagnetic Compatibility and Asia-Pacific Symposium on Electromagnetic Compatibility (EMC/APEMC)*, 129, 2018.
9. Wang, L., W. Hong, L. Deng, S. Li, S. Uddin, H. Tian, and D. Chen, "Flexible broadband achromatic microwave metalens design using polynomial fitting method," *Proceedings of Asia Microwave Conference (APMC)*, 1384–1386, 2018.
10. Azad, K. A., V. A. Efimov, S. Ghosh, J. Singleton, J. A. Taylor, and H. Chen, "Ultra-thin metasurface microwave flat lens for broadband applications," *Applied Physics Letters*, Vol. 110, No. 22, 1–5, 2017.
11. Zhang, Y., X. Zhang, et al., "Moving train imaging by ground-based Ka-band radar," *Loughborough Antenna and Propagation Conference (LAPC)*, 413–416, Loughborough, UK, Nov. 16–18, 2009.
12. Zhang, X., W. Zhai, and Y. Zhang, "A prototype for stepped-frequency SAR dechirp imaging system and experimental verification," *2009 Asia-Pacific Microwave Conference (APMC)*, Singapore, Dec. 7–10, 2009.
13. Zhang, X. and Y. Zhang, "High-resolution imaging of a moving train by ground-based radar with compressive sensing," *Electronic Letters*, Vol. 46, No. 7, 529–531, Apr. 2010.
14. Winston, R., J. Minano, and P. Benitez, *Nonimaging Optics*, Academic Press, 2004.
15. Pourahmadazar, J. and T. Denidni, "Towards millimeter-wavelength: Transmission-mode fresnel-zone plate lens antennas using plastic material porosity control in homogeneous medium," *Scientific Reports*, Vol. 8, No. 5300, 1–14, 2018.
16. Öziş, E., A. V. Osipov, and T. F. Eibert, "A semi-analytical approach for fast design of microwave metasheets with circular metal rings on dielectric substrates," *Progress In Electromagnetics Research C*, Vol. 88, 13–25, 2018.
17. Glassner, S. A., *An Introduction to Ray Tracing*, Academic Press, USA, 1989.
18. Balanis, A. C., *Advanced Engineering Electromagnetics*, Wiley, Hoboken, 2012.
19. Durgun, C. A. and M. Kuzuoğlu, "Computation of physical optics integral by Levin's integration algorithm," *Progress In Electromagnetics Research M*, Vol. 6, 59–74, 2009.
20. Ludwig, A. C., "Computation of radiation patterns involving numerical double integration," *IEEE Transactions on Antennas and Propagation*, Vol. 16, No. 6, 767–769, 1968.
21. Dos Santos, M. L. X. and R. N. Rabelo, "On the Ludwig integration algorithm for triangular subregions," *Proceedings of the IEEE*, Vol. 74, No. 10, 1455–1456, 1986.
22. Youssef, N. N., "Radar cross section of complex targets," *Proc. IEEE*, Vol. 77, 722–734, 1989.
23. Öziş, E., V. A. Osipov, and F. T. Eibert, "Physical optics and full-wave simulations of transmission of electromagnetic fields through electrically large planar metasheets," *Advances in Radio Science*, Vol. 15, 29–35, 2017.
24. Osipov, A. V. and S. A. Tretyakov, *Modern Electromagnetic Scattering Theory with Applications*, Wiley, United Kingdom, 2017.
25. Crabtree, D. G., "A numerical quadrature technique for physical optics scattering analysis," *IEEE Transactions on Magnetics*, Vol. 27, No. 5, 4291–4294, 1991.
26. Carluccio, G. and M. Albani, "Efficient adaptive numerical integration algorithms for the evaluation of surface radiation integrals in the high-frequency regime," *Radio Science*, Vol. 46, No. 5, 1–8, 2011.